

Entangling single atoms over 33 km telecom fibre

Tim van Leent (✉ t.van.leent@physik.uni-muenchen.de)

Ludwig-Maximilians-Universität München

Matthias Bock

Universität des Saarlandes

Florian Fertig

LMU München

Robert Garthoff

LMU München

Sebastian Eppelt

LMU München

Yiru Zhou

Ludwig-Maximilians-Universität München

Pooja Malik

Ludwig-Maximilians-Universität München

Matthias Seubert

Ludwig-Maximilians-Universität München

Tobias Bauer

Universität des Saarlandes <https://orcid.org/0000-0003-4802-4215>

Wenjamin Rosenfeld

Ludwig-Maximilians-Universität München

Wei Zhang

LMU München

Christoph Becher

Universität des Saarlandes <https://orcid.org/0000-0003-4645-6882>

Harald Weinfurter

LMU München

Physical Sciences - Article

Keywords:

Posted Date: January 13th, 2022

DOI: <https://doi.org/10.21203/rs.3.rs-1145833/v1>

License:  This work is licensed under a Creative Commons Attribution 4.0 International License.

[Read Full License](#)

Version of Record: A version of this preprint was published at Nature on July 6th, 2022. See the published version at <https://doi.org/10.1038/s41586-022-04764-4>.

Entangling single atoms over 33 km telecom fibre

Tim van Leent,^{1,2,*} Matthias Bock,^{3,*} Florian Fertig,^{1,2,*} Robert Garthoff,^{1,2} Sebastian Eppelt,^{1,2} Yiru Zhou,^{1,2} Pooja Malik,^{1,2} Matthias Seubert,^{1,2} Tobias Bauer,³ Wenjamin Rosenfeld,^{1,2} Wei Zhang,^{1,2,†} Christoph Becher,^{3,‡} and Harald Weinfurter^{1,2,4,§}

¹*Fakultät für Physik, Ludwig-Maximilians-Universität München, Schellingstr. 4, 80799 München, Germany*

²*Munich Center for Quantum Science and Technology (MCQST), Schellingstr. 4, 80799 München, Germany*

³*Fachrichtung Physik, Universität des Saarlandes, Campus E2.6, 66123 Saarbrücken, Germany*

⁴*Max-Planck Institut für Quantenoptik, Hans-Kopfermann-Str. 1, 85748 Garching, Germany*

(Dated: December 24, 2021)

Heralded entanglement between distant quantum memories is the key resource for quantum networks. Based on quantum repeater protocols, these networks will facilitate efficient large-scale quantum communication and distributed quantum computing. However, despite vast efforts, long-distance fibre based network links have not been realized yet. Here we present results demonstrating heralded entanglement between two independent, remote single-atom quantum memories generated over fibre links with a total length up to 33 km. To overcome the attenuation losses in the long optical fibres of photons initially emitted by the Rubidium quantum memories, we employ polarization-preserving quantum frequency conversion to the low loss telecom band. The presented work represents a milestone towards the realization of efficient quantum network links.

Sharing entanglement between distant quantum systems is a crucial ingredient for the realization of quantum networks^{1,2}. Photons are the tool of choice to mediate entanglement distribution, typically either via controlled light-matter interaction with local memories^{3,4}, or, as it also will be used here, via entanglement swapping from two pairs of entangled photon-memory states^{5–8}. Innovative applications of such networks include distributed quantum computing⁹ and device-independent quantum key distribution¹⁰. Since attenuation losses in the distribution process are inevitable, quantum repeaters will be essential to efficiently distribute entanglement via intermediate nodes.

To minimize absorption along the quantum channel and thus to maximize the distance between neighbouring nodes in quantum networks employing the readily available fibre infrastructure, it is necessary to convert light to telecom wavelengths^{11–15}. Light-matter entanglement distributed at the low loss telecom band has recently been demonstrated for various types of quantum memories, including NV-centres, ions, atoms, and atomic ensembles^{16–19}, even over tens of kilometres of fibre^{20,21}. This was mainly enabled by novel quantum frequency converters^{16,17}, which, while preserving the photonic polarization, have reached external device conversion efficiencies as high as 57%²¹.

For future quantum communication and repeater scenarios, it is vital that the nodes are independent and distant, employ long-lived quantum memories, and, at the same time, provide the availability of heralded entanglement, i.e., there is a well defined signal available that the entanglement distribution succeeded. So far, this has

been limited to fibre lengths up to 1.7 km^{22,23}. Recently, great progress was made by demonstrating telecom-heralded entanglement between atomic ensembles²⁴ and multimode solid-state quantum memories²⁵, however, having limited memory storage times and not employing independent nodes.

Here we report on the distribution of entanglement between two remote quantum nodes—⁸⁷Rb atoms trapped and manipulated independently at locations 400 m apart—generated over fibre links with a length of up to 33 km. The scheme begins with entangling the spin state of an atom with the polarization state of a photon in each node. Subsequently, the photons emitted by the atoms at 780 nm are converted to telecom wavelength and transferred over several kilometres of fibre to a middle station, where a Bell-state measurement is performed to swap the entanglement to the atoms. We analyse the heralded entanglement between the atoms for different fibre link lengths using correlation measurements of the atom-atom state along three bases. The atoms are analysed after a delay allowing for two-way communication to the middle station over the full fibre link length to realistically evaluate the performance for long fibre lengths.

QUANTUM NETWORK LINK WITH TELECOM INTERFACES

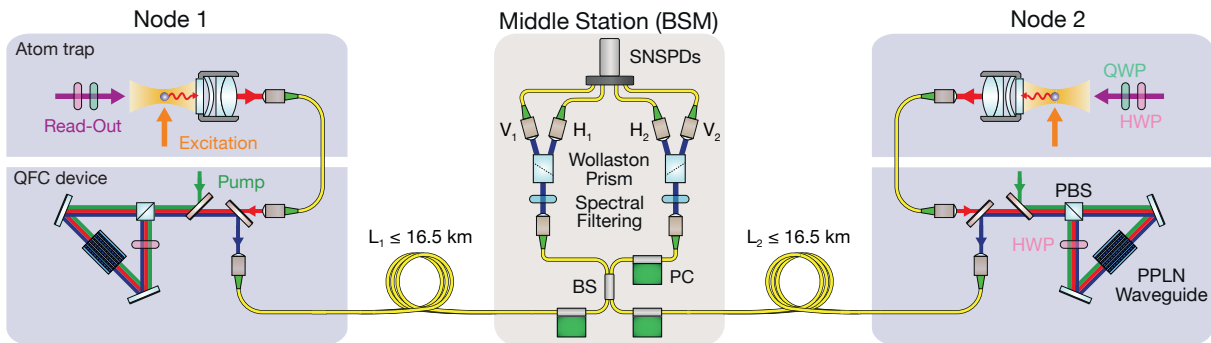
Our experiment consists of two similar, independent nodes and a middle station, which all are located in different laboratories, as illustrated in Fig. 1. The shortest possible fibre connection from Node 1 (Node 2) to the middle station equals 50 m (750 m), longer fibre links are realized by inserting additional fibres on spools. The fibre length to the middle station is denoted as L_1 (L_2), with the total link length $L = L_1 + L_2$. In both nodes, a single, optically trapped ⁸⁷Rb atom acts as a quantum memory²⁶, where a qubit is encoded in the Zeeman

* These authors contributed equally

† Email: wei.zhang@xjtu.edu.cn; Present address: Xi’An Jiao Tong University, Xi’An ShannXi, China

‡ Email: christoph.becher@physik.uni-saarland.de

§ Email: h.w@lmu.de



74

75 **FIG. 1. Schematic of the experimental setup.** In each node, located in buildings 400 m apart, a single ^{87}Rb atom is loaded
 76 in an optical dipole trap. Both atoms are synchronously excited to the state $5^2P_{3/2}|F'=0, m_F=0\rangle$ to generate atom-photon
 77 entanglement in the subsequent spontaneous decay. The single photons emitted at a wavelength of 780 nm are collected using
 78 high-NA objectives and coupled into single mode fibres leading to the QFC devices. There, they are converted to telecom
 79 wavelength ($\lambda = 1517$ nm) via difference frequency generation (DFG) in a PPLN waveguide located in a Sagnac interferometer
 80 type setup. This particular configuration fully maintains the polarization quantum state of the photon. The converted photons
 81 are guided to a middle station via fibre links with lengths up to 16.5 km, where the entanglement is swapped to the atoms via a
 82 Bell state measurement (BSM). After successfully generating atom-atom entanglement, the atoms are analysed independently
 83 by a read-out pulse of which the polarization, set by a half-wave plate (HWP) and quarter-wave plate (QWP), defines the
 84 measurement setting.

97 substates of the $5^2S_{1/2}|F=1, m_F=\pm 1\rangle$ ground state,
 98 with $m_F = +1$ and $m_F = -1$ further denoted as $|\uparrow\rangle_z$
 99 and $|\downarrow\rangle_z$, respectively.

100 The experimental sequence starts by generating atom-
 101 photon entanglement in each node²⁷. For this pur-
 102 pose, the atoms are prepared in the initial state
 103 $5^2S_{1/2}|F=1, m_F=0\rangle$ via optical pumping and excited
 104 to the state $5^2P_{3/2}|F'=0, m_F=0\rangle$. During the spon-
 105 taneous decay back to the ground state the atomic spin
 106 state becomes entangled with the polarization of the re-
 107 spective emitted photon at 780 nm due to the conserva-
 108 tion of angular momentum. This results in the entangled
 109 atom-photon state $|\Psi\rangle_{AP} = 1/\sqrt{2}(|\downarrow\rangle_z|L\rangle + |\uparrow\rangle_z|R\rangle) =$
 110 $1/\sqrt{2}(|\downarrow\rangle_x|V\rangle + |\uparrow\rangle_x|H\rangle)$, where $|L\rangle$ and $|R\rangle$ denote left-
 111 and right-circular photonic polarization states, $|H\rangle$ and
 112 $|V\rangle$ denote horizontal and vertical linear polarizations.
 113 A custom made high-NA objective is used to collect the
 114 atomic fluorescence into single-mode fibres.

115 Photons with a wavelength of 780 nm now would suf-
 116 fer an attenuation by a factor of 10 after propagation
 117 through 2.5 km fibre. To overcome such high attenu-
 118 ation loss, we employ polarization-perserving quantum
 119 frequency conversion (QFC) to transform the wavelength
 120 of the photons to the telecom S band, where one ex-
 121 pects attenuation by a factor of 10 only after about 50
 122 km transmission. The QFC is realized by mixing the
 123 photons with a strong pump field at 1607 nm inside a
 124 nonlinear waveguide crystal, converting the wavelength
 125 to 1517 nm via difference frequency generation. Various
 126 spectral filtering stages, including a narrow band filter
 127 cavity (27 MHz FWHM), separate the single photons
 128 from the strong pump field and the anti-stokes Raman
 129 background originating from this field. In the shortest fi-
 130 bre configuration this results in a background of approx-

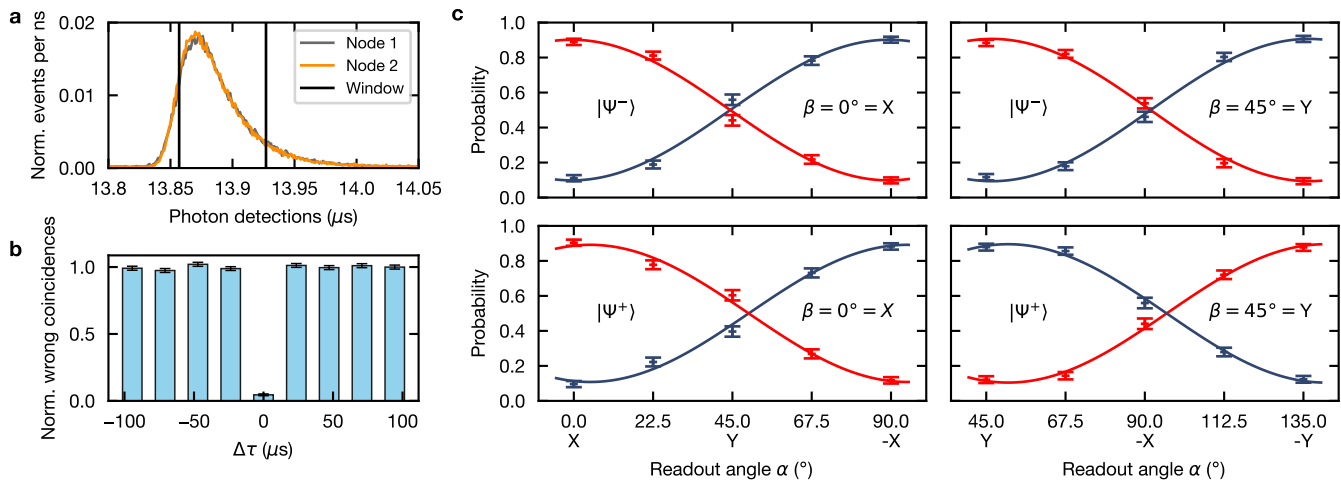
131 imately 160 and 170 cps registered at the middle station
 132 for light from Node 1 and 2, respectively. Both converters
 133 achieve an external device efficiency of 57%. The pump
 134 light is conveniently distributed to the nodes using the
 135 telecom fibre network and hence ensures indistinguish-
 136 able frequencies of the single photons after conversion.
 137 For more details about the QFC system and an analysis
 138 of the atom-photon entanglement distribution at telecom
 139 wavelength see Ref.²¹ and Methods.

140 After frequency conversion, the photons are guided
 141 to the middle station with fibres of different lengths
 142 where a Bell-state measurement (BSM) swaps the en-
 143 tanglement to the atoms^{6,23}. The fidelity of the BSM,
 144 and hence of the entanglement swapping protocol, is de-
 145 termined by the photons temporal, spectral, and spa-
 146 tial indistinguishability²⁸. This is optimized by different
 147 means, first, the photons impinge on a balanced, single-
 148 mode fibre beam splitter to guarantee a perfect spatial
 149 overlap. Second, the entanglement generation process in
 150 the nodes is synchronized to < 300 ps, which is much
 151 smaller than the coherence time of the photons deter-
 152 mined by the lifetime of the excited state of 26.2 ns. And
 153 third, polarization drifts in the long fibres are compen-
 154 sated using an automated polarization control²⁹. The
 155 photons are detected with four superconducting nanowire
 156 single-photon detectors (SNSPD), which all have an effi-
 157 ciency of $> 85\%$ and a darkcount rate of < 65 cps.

158 The employed BSM setup analyses the photons in the
 159 H/V basis and hence heralds the following two Bell states

$$|\Psi^\pm\rangle = \frac{1}{\sqrt{2}}(|\uparrow\rangle_x|\downarrow\rangle_x \pm |\downarrow\rangle_x|\uparrow\rangle_x). \quad (1)$$

170 Two-photon coincidences are triggered within a hard-
 171 wired 208 ns long window which sends this heralding



158

159 **FIG. 2. Characterization of the atom-atom entanglement for a fibre length of $L = 6$ km.** **a**, Detection time histogram
 160 of the photons originating from Node 1 and 2 relative to the time of excitation in Node 1. For the indicated acceptance window,
 161 we observe a SBR of 58 and 65 for Node 1 and 2, respectively. The temporal overlap of the two photons is > 0.98 . **b**, Two-
 162 photon interference based on the Hong-Ou-Mandel effect. Shown is the normalized number of wrong coincidences for various
 163 time differences between the two photon wave-packets ($\Delta\tau$). **c**, Atom-atom state correlations for the $|\Psi^-\rangle$ (top) and $|\Psi^+\rangle$
 164 (bottom) states. The correlation probability of the measurement outcome in the nodes is shown in blue, while the anti-
 165 correlation probabilities are marked in red. The data are fitted with sinusoidal functions resulting in an estimated fidelity for
 166 $|\Psi^-\rangle$ and $|\Psi^+\rangle$ relative to a maximally entangled state of 0.826(18) and 0.806(20), respectively. The errorbars in all figures
 167 indicate statistical errors of one standard deviation.

172 signal back to the nodes. The signal is delayed electron- 199
 173 ically by $t \geq \ell/\frac{2}{3}c$ to simulate the signalling time back 200
 174 to the nodes, where $\frac{2}{3}c$ approximates the speed of light 201
 175 in an optical fibre and ℓ equals L_1 or L_2 for Node 1 or 202
 176 2, respectively. Although lowering the observed final 203
 177 fidelity, this delay is essential to study the performance of 204
 178 the quantum network link in a realistic scenario. 205

179 The quantum state of the atomic memories is finally 206
 180 analysed with a state-selective ionization scheme, 207
 181 whereby the state selectivity is controlled by the polar- 208
 182 ization of a readout laser pulse²¹. Both memories have 209
 183 a coherence time T_2 of approximately 330 μs , which is 210
 184 achieved by active stabilization of magnetic fields (< 0.5 211
 185 mG) and applying a bias field of tens of milligauss along 212
 186 the y axis. Currently, the coherence time is limited by 213
 187 magnetic field fluctuations along the bias field direction 214
 188 and a position-dependent dephasing originating from lon- 215
 189 gitudinal field components of the strongly focussed dipole 216
 190 trap. For more details and a simulation of the limiting 217
 191 decoherence mechanisms see Methods. 218

192 ENTANGLEMENT DISTRIBUTION AT 193 TELECOM WAVELENGTH

194 The evaluation of the entanglement distribution over long 224
 195 fibre links is detailed first exemplarily for a fibre con- 225
 196 figuration of $L = 6$ km. The entanglement generation 226
 197 rate is determined by three factors: the probability of 227
 198 generating an entangled state between the atoms after a 228

199 synchronized excitation attempt, which is predominantly 200
 201 reduced by the photon collection efficiency in the nodes 202
 202 and amounts to $3.66 \cdot 10^{-6}$; the repetition rate of 30.8 203
 203 kHz, which is mainly limited by the communication time 204
 204 between the nodes; and the duty cycle of approximately 205
 205 $1/2$ which includes the fraction of time that an atom is 206
 206 present in both traps. This leads to an event rate of 207
 207 $1/19 \text{ s}^{-1}$ resulting in $N = 10290$ entanglement genera- 208
 208 tion events within 54 hours. 209

208 Facing Raman background from two QFC devices 209
 209 in addition to detector dark counts, a 70 ns photon 210
 210 acceptance window is applied during the data post- 211
 211 processing, as shown in Fig. 2a. This results in a signal- 212
 212 to-background ratio (SBR) of 58 (65) for detecting a 213
 213 single photon from Node 1 (Node 2), which is significantly 214
 214 higher than in a previously reported work (Ref.²¹) thanks 215
 215 to a more favourable pump-signal frequency combination 216
 216 with respect to the Raman background. For the coinci- 217
 217 dence detections this leads to a SBR of 48 while accepting 218
 218 approximately 65% of the recorded events. 219

219 The quality of the two-photon interference of the con- 220
 220 verted photons is quantified by the relative occurrence 221
 221 of wrong detector coincidences⁶. These coincidences, 222
 222 i.e., (V_1, V_2) and (H_1, H_2) , should not occur for perfectly 223
 223 interfering, fully-unpolarized photons. For temporally 224
 224 well overlapping photons ($\Delta\tau = 0$), but without back- 225
 225 ground correction, this results in an interference contrast 226
 226 of 0.955(7) (Fig. 2b). Here, double-excitation events in 227
 227 the nodes reduce the indistinguishability of the detected 228
 228 photons by changing the temporal shape. By rejecting

early detection events, this effect is reduced at the cost of a lower event rate. For more details see Methods.

To evaluate the atom-atom entanglement we measured the atomic spin states in the two linear bases, X and Y . For this, the polarization analysis angle in Node 2 was set to $\beta = 0^\circ = X$ and $\beta = 45^\circ = Y$, while the analysis angle in Node 1 was varied over 90° in steps of 22.5° starting from $\alpha = 0^\circ = X$ and $\alpha = 45^\circ = Y$, respectively. The atom in Node 1 (Node 2) was analysed at $t_1 = 28.5 \mu\text{s}$ ($t_2 = 35.5 \mu\text{s}$) after the respective excitation pulse. The resulting atomic state correlation probabilities $P_{corr} = (N_{\uparrow\uparrow}^{\alpha,\beta} + N_{\downarrow\downarrow}^{\alpha,\beta})/N^{\alpha,\beta}$ and anti-correlation probabilities $P_{acorr} = (N_{\uparrow\downarrow}^{\alpha,\beta} + N_{\downarrow\uparrow}^{\alpha,\beta})/N^{\alpha,\beta}$ are shown in Fig. 2c. The data are fitted with sinusoidal curves giving average visibilities of $\bar{V} = 0.804(20)$ for $|\Psi^-\rangle$ and $\bar{V} = 0.784(23)$ for $|\Psi^+\rangle$. To estimate the state fidelity we need to consider that the third ground state ($5^2S_{1/2}|F = 1, m_F = 0\rangle$) can be populated, hence operating effectively in a 3×3 state space. Therefore, a lower bound on the fidelity is given by $\mathcal{F} \geq \frac{1}{9} + \frac{8}{9}\bar{V} = 0.826(18)$ for $|\Psi^-\rangle$ and $0.806(20)$ for $|\Psi^+\rangle$, relative to a maximally entangled state. Furthermore, the chosen analysis angles allow to evaluate the Clauser-Horne-Shimony-Holt (CHSH) S value³⁰ for the settings $\alpha = 22.5^\circ$, $\beta = 0^\circ$; $\alpha' = 67.5^\circ$, $\beta = 0^\circ$; $\alpha' = 67.5^\circ$, $\beta = 45^\circ$; and $\alpha'' = 112.5^\circ$, $\beta' = 45^\circ$, whereby α'' replaces $\alpha = 22.5^\circ$. This results in an observed value of $S = 2.244(63)$, violating the limit of 2 with 3.9σ .

ENTANGLEMENT DISTRIBUTION OVER UP TO 33 KM FIBRE

To determine the effect of long fibre links, we performed a series of measurements generating and observing atom-atom entanglement in fibre configurations with a length L of 6, 11, 23, and 33 km. For longer links, the event rate reduces due to both the signal attenuation of 0.22 dB/km and the longer communication times. At 33 km, this results in a repetition rate of 9.7 kHz, a success probability of $1.22 \cdot 10^{-6}$, and an event rate of $1/208 \text{ s}^{-1}$. In these measurements, the entanglement fidelity relative to maximally entangled states was analysed by measurements along three bases (X , Y , and Z). Fig. 3 shows the probability of correlated measurement outcomes in the nodes for each measurement setting combination and fibre configuration.

The fidelity of the observed states is estimated by first determining the contrast in the three measurement bases independently. This is done by taking the absolute difference of the two measured correlation probabilities, $E_k = |P_{k,k} - P_{-k,k}|$ for $k \in \{X, Y, Z\}$, from which the average contrast is computed as $\bar{E} = (E_X + E_Y + E_Z)/3$. When averaging over the observed states $|\Psi^\pm\rangle$ —which show within our measurement precision similar visibilities—and again assuming the 3×3 state space, this results in a lower bound on the fidelities $\mathcal{F} = 0.830(10)$, $0.799(11)$, $0.719(12)$, and $0.622(15)$ relative to maximally entangled

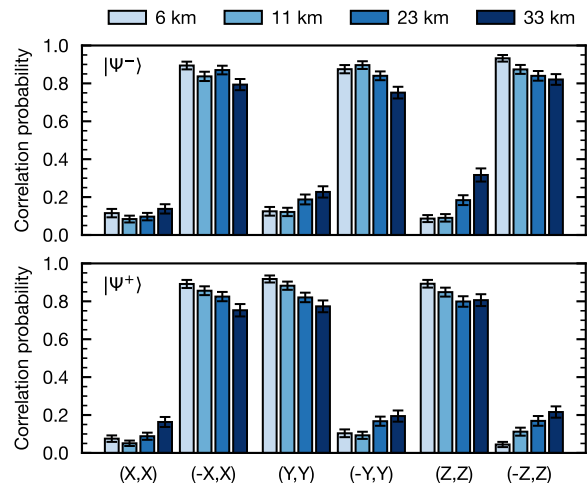
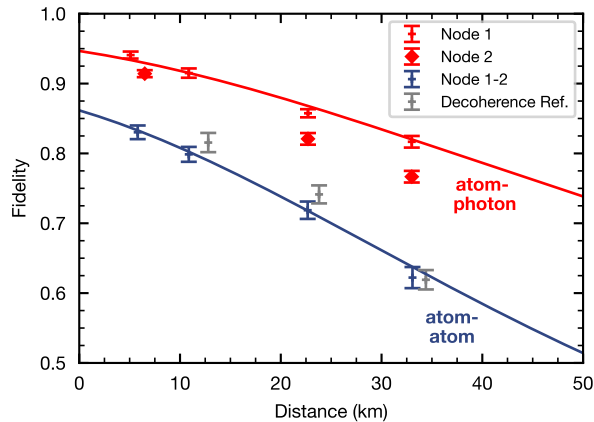


FIG. 3. **Observation of heralded atom-atom entanglement generated over long fibre links.** Correlations between the measurement results when analysing the generated atom-atom Bell states for various link lengths. For each link, the states were analysed in 3 conjugate bases (Node 1, Node 2), whereby the correlation probability of the measurement result in the nodes equals $P_{corr} = (N_{\uparrow\uparrow} + N_{\downarrow\downarrow})/(N_{\uparrow\uparrow} + N_{\downarrow\downarrow} + N_{\uparrow\downarrow} + N_{\downarrow\uparrow})$. For the different fibre lengths (short to long) 4281, 4271, 4153, and 3022 entanglement events were recorded within a measurement time of 11, 65, 97, and 175 hours. Of these events, 62-72% was within the two-photon coincidence acceptance window, resulting in $N = 185$ to 225 events per data-point.

states for L equals 6, 11, 23, and 33 km, respectively. The estimated fidelity for the 6 km fibre configuration is in good agreement with the fidelity estimated from the fringe measurements in two bases presented before. Moreover, all observed fidelities clearly exceed the bound of 0.5 and hence witness an entangled state.

The observed fidelities are shown in dependence of the fibre link length in Fig. 4, where also the measured atom-photon entanglement fidelities for states shared between the nodes and the middle station are shown for completeness. The atom-atom state fidelity for different fibre lengths $\mathcal{F}(L)$ is modelled based on simulations of the generation and evolution of the two atom-photon states, which are shown with solid lines. We estimate the visibility of the atom-atom state by the product of the two atom-photon visibilities and the interference contrast of the BSM³¹. Evidently, decoherence of the atomic states dominates the loss in fidelity for longer fibre links. For $L = 33$ km, the states were analysed 171 μs and 178 μs after excitation in Node 1 and 2, respectively, which approaches the coherence time of the states. In contrast, the SBR is robust to an increase in fibre length since both the single photons as well as the QFC background are attenuated in the long links. A minor reduction in SBR (42 for $L = 33$ km) is explained by relatively more detector dark counts and can be solved by installing de-



304

305 **FIG. 4. Observed entanglement fidelity for various link**
 306 **lengths.** Overview of the observed atom-atom fidelities for
 307 different fibre configurations (blue). For completeness, the ob-
 308 served atom-photon fidelities of the states between the nodes
 309 and the middle station (red), with $L = 2 \cdot L_i$, are given (see
 310 Methods). The solid lines are simulations based on a model
 311 taking into account the decoherence of the atomic memories,
 312 see Methods. The gray points are reference measurements
 313 of the atom-atom state decoherence, without long fibres, but
 314 with corresponding readout delay.

335 tectors with lower dark counts. Also, polarization drifts
 336 are comparably well compensated in all link configura-
 337 tions, see Methods.

338 To verify that the memory decoherence limits the loss
 339 in fidelity for long fibre links, we performed a series of

340 measurements without additional fibres inserted, how-
 341 ever, with the memory readout times electronically de-
 342 layed according to the long fibre links. The observed
 343 fidelities are shown in gray in Fig. 4 at $L = \frac{2}{3}c(t_1 + t_2)/2$
 344 (matching the two-way communication time to the mid-
 345 dle station for distance L) and show, within the mea-
 346 surement accuracy, no difference in observed fidelity com-
 347 pared to the configuration with long fibres.

348

DISCUSSION AND OUTLOOK

349 The results clearly indicate the feasibility of turning to
 350 large-scale quantum networks by facilitating an increase
 351 in line-of-sight separation of the nodes to tens of kilo-
 352 metres. Possible improvements include increasing the
 353 coherence time of the atomic states by implementing a
 354 new trap geometry to mitigate the position-dependent
 355 dephasing in combination with a state-transfer to a qubit
 356 encoding less sensitive to magnetic fields³². This will al-
 357 low to generate entanglement of quantum memories on a
 358 suburban scale with a high fidelity.

359 To conclude, employing efficient telecom interfaces in
 360 our nodes enabled the generation of heralded entangle-
 361 ment between two atomic quantum memories over fibre
 362 links with a length up to 33 km. The analysis of the
 363 results clearly shows that improvements on the memory
 364 coherence time are mandatory but will allow to entangle
 365 two atomic quantum memories with a fidelity better
 366 than 80% over fibre lengths up to 100 km, thereby
 367 paving the way towards long-distance entanglement
 368 distribution for future quantum repeater networks.

369

-
- 370 [1] H-J Briegel, Wolfgang Dür, Juan I Cirac, and Peter 393
 371 Zoller. Quantum repeaters: the role of imperfect local 394
 372 operations in quantum communication. *Physical Review 395*
 373 *Letters*, 81(26):5932, 1998. 396
 374 [2] H Jeff Kimble. The quantum internet. *Nature*, 397
 375 453(7198):1023, 2008. 398
 376 [3] Manuel Brekenfeld, Dominik Niemietz, Joseph Dale 399
 377 Christesen, and Gerhard Rempe. A quantum network 400
 378 node with crossed optical fibre cavities. *Nature Physics*, 401
 379 16(6):647–651, 2020. 402
 380 [4] Severin Daiss, Stefan Langenfeld, Stephan Welte, 403
 381 Emanuele Distante, Philip Thomas, Lukas Hartung, 404
 382 Olivier Morin, and Gerhard Rempe. A quantum-logic 405
 383 gate between distant quantum-network modules. *Sci- 406*
 384 *ence*, 371(6529):614–617, 2021. 407
 385 [5] Marek Zukowski, Anton Zeilinger, Michael A Horne, and 408
 386 Aarthur K Ekert. "event-ready-detectors" bell experi- 409
 387 ment via entanglement swapping. *Physical Review Let- 410*
 388 *ters*, 71(26), 1993. 411
 389 [6] Julian Hofmann, Michael Krug, Norbert Ortengel, Lea 412
 390 Gérard, Markus Weber, Wenjamin Rosenfeld, and Har- 413
 391 ald Weinfurter. Heralded entanglement between widely 414
 392 separated atoms. *Science*, 337(6090):72–75, 2012. 415
- [7] Matteo Pompili, Sophie LN Hermans, Simon Baier, 416
 Hans KC Beukers, Peter C Humphreys, Raymond N 417
 Schouten, Raymond FL Vermeulen, Marijn J Tiggelman, 418
 Laura dos Santos Martins, Bas Dirkse, et al. Realization 419
 of a multinode quantum network of remote solid-state 420
 qubits. *Science*, 372(6539):259–264, 2021. 421
 [8] Xiao Liu, Jun Hu, Zong-Feng Li, Xue Li, Pei-Yun Li, 422
 Peng-Jun Liang, Zong-Quan Zhou, Chuan-Feng Li, and 423
 Guang-Can Guo. Heralded entanglement distribution 424
 between two absorptive quantum memories. *Nature*, 425
 594(7861):41–45, 2021. 426
 [9] Daniele Cuomo, Marcello Caleffi, and Angela Sara Cac- 427
 ciapuoti. Towards a distributed quantum computing 428
 ecosystem. *IET Quantum Communication*, 1(1):3–8, 429
 2020. 430
 [10] Antonio Acín, Nicolas Brunner, Nicolas Gisin, Serge 431
 Massar, Stefano Pironio, and Valerio Scarani. Device- 432
 independent security of quantum cryptography 433
 against collective attacks. *Physical Review Letters*, 434
 98(23):230501, 2007. 435
 [11] Sebastian Zaske, Andreas Lenhard, Christian A Keßler, 436
 Jan Kettler, Christian Hepp, Carsten Arend, Roland Al- 437
 brecht, Wolfgang-Michael Schulz, Michael Jetter, Peter 438

- 416 Michler, et al. Visible-to-telecom quantum frequency 480
 417 conversion of light from a single quantum emitter. *Phys-* 481
 418 *ical Review Letters*, 109(14):147404, 2012. 482
- 419 [12] Serkan Ates, Imad Agha, Angelo Gulinatti, Ivan Rech, 483
 420 Matthew T Rakher, Antonio Badolato, and Kartik Srini- 484
 421 vasan. Two-photon interference using background-free 485
 422 quantum frequency conversion of single photons emit- 486
 423 ted by an inas quantum dot. *Physical Review Letters*, 487
 424 109(14):147405, 2012. 488
- 425 [13] Kristiaan De Greve, Leo Yu, Peter L McMahon, Jason S 489
 426 Pelc, Chandra M Natarajan, Na Young Kim, Eisuke Abe, 490
 427 Sebastian Maier, Christian Schneider, Martin Kamp, 491
 428 et al. Quantum-dot spin-photon entanglement via fre- 492
 429 quency downconversion to telecom wavelength. *Nature*, 493
 430 491(7424):421, 2012. 494
- 431 [14] Rikizo Ikuta, Yoshiaki Kusaka, Tsuyoshi Kitano, Hiro- 495
 432 shi Kato, Takashi Yamamoto, Masato Koashi, and 496
 433 Nobuyuki Imoto. Wide-band quantum interface for 497
 434 visible-to-telecommunication wavelength conversion. *Na-* 498
 435 *ture Communications*, 2:537, 2011. 499
- 436 [15] Nicolas Maring, Pau Farrera, Kutlu Kutluer, Margherita 500
 437 Mazzera, Georg Heinze, and Hugues de Riedmatten. 501
 438 Photonic quantum state transfer between a cold atomic 502
 439 gas and a crystal. *Nature*, 551(7681):485–488, 2017. 503
- 440 [16] Matthias Bock, Pascal Eich, Stephan Kucera, Matthias 504
 441 Kreis, Andreas Lenhard, Christoph Becher, and Jürgen 505
 442 Eschner. High-fidelity entanglement between a trapped 506
 443 ion and a telecom photon via quantum frequency conver- 507
 444 sion. *Nature Communications*, 9(1):1998, 2018. 508
- 445 [17] Rikizo Ikuta, Toshiaki Kobayashi, Tetsuo Kawakami, 509
 446 Shigehito Miki, Masahiro Yabuno, Taro Yamashita, Hi- 510
 447 rotaka Terai, Masato Koashi, Tetsuya Mukai, Takashi 511
 448 Yamamoto, et al. Polarization insensitive frequency con- 512
 449 version for an atom-photon entanglement distribution via 513
 450 a telecom network. *Nature Communications*, 9(1):1997, 514
 451 2018. 515
- 452 [18] Y. O. Dudin, A. G. Radnaev, Ran Zhao, J. Z. Blumoff, 516
 453 T. A. B. Kennedy, and Alex Kuzmich. Entanglement of 517
 454 light-shift compensated atomic spin waves with telecom 518
 455 light. *Physical Review Letters*, 105(26):260502, 2010. 519
- 456 [19] Anna Tchebotareva, Sophie L. N. Hermans, Peter C. 520
 457 Humphreys, Dirk Voigt, Peter J. Harmsma, Lun K. 521
 458 Cheng, Ad L. Verlaan, Niels Dijkhuizen, Wim de Jong, 522
 459 Anaïs Dréau, and Ronald Hanson. Entanglement be- 523
 460 tween a diamond spin qubit and a photonic time-bin 524
 461 qubit at telecom wavelength. *Physical Review Letters*,
 462 123:063601, Aug 2019.
- 463 [20] V Krutyanskiy, M Meraner, J Schupp, V Krcmarsky, 525
 464 H Hainzer, and BP Lanyon. Light-matter entanglement
 465 over 50 km of optical fibre. *npj Quantum Information*,
 466 5(1):1–5, 2019.
- 467 [21] Tim van Leent, Matthias Bock, Robert Garthoff, Kai Re-
 468 deker, Wei Zhang, Tobias Bauer, Wenjamin Rosenfeld,
 469 Christoph Becher, and Harald Weinfurter. Long-distance
 470 distribution of atom-photon entanglement at telecom
 471 wavelength. *Physical Review Letters*, 124(1):010510,
 472 2020.
- 473 [22] Bas Hensen, Hannes Bernien, Anaïs E Dréau, Andreas
 474 Reiserer, Norbert Kalb, Machiel S Blok, Just Ruitenber,
 475 Raymond FL Vermeulen, Raymond N Schouten, Carlos
 476 Abellán, et al. Loophole-free bell inequality violation
 477 using electron spins separated by 1.3 kilometres. *Nature*,
 478 526(7575):682–686, 2015.
- 479 [23] Wenjamin Rosenfeld, Daniel Burchardt, Robert
 480 Garthoff, Kai Redeker, Norbert Ortegel, Markus Rau,
 481 and Harald Weinfurter. Event-ready bell test using
 482 entangled atoms simultaneously closing detection and lo-
 483 cality loopholes. *Physical Review Letters*, 119(1):010402,
 484 2017.
- 485 [24] Yong Yu, Fei Ma, Xi-Yu Luo, Bo Jing, Peng-Fei Sun,
 486 Ren-Zhou Fang, Chao-Wei Yang, Hui Liu, Ming-Yang
 487 Zheng, Xiu-Ping Xie, et al. Entanglement of two quan-
 488 tum memories via fibres over dozens of kilometres. *Na-*
 489 *ture*, 578(7794):240–245, 2020.
- 490 [25] Dario Lago-Rivera, Samuele Grandi, Jelena V Rakonjac,
 491 Alessandro Seri, and Hugues de Riedmatten. Telecom-
 492 heralded entanglement between multimode solid-state
 493 quantum memories. *Nature*, 594(7861):37–40, 2021.
- 494 [26] Markus Weber, Jürgen Volz, Karen Saucke, Christian
 495 Kurtsiefer, and Harald Weinfurter. Analysis of a single-
 496 atom dipole trap. *Physical Review A*, 73(4):043406, 2006.
- 497 [27] Jürgen Volz, Markus Weber, Daniel Schlenk, Wenjamin
 498 Rosenfeld, Johannes Vrana, Karen Saucke, Christian
 499 Kurtsiefer, and Harald Weinfurter. Observation of entan-
 500 glement of a single photon with a trapped atom. *Physical*
 501 *Review Letters*, 96(3):030404, 2006.
- 502 [28] Wenjamin Rosenfeld, Julian Hofmann, Norbert Ortegel,
 503 Michael Krug, Florian Henkel, Ch Kurtsiefer, Markus
 504 Weber, and Harald Weinfurter. Towards high-fidelity in-
 505 terference of photons emitted by two remotely trapped
 506 rb-87 atoms. *Optics and Spectroscopy*, 111(4):535–539,
 507 2011.
- 508 [29] W Rosenfeld, F Hocke, F Henkel, M Krug, J Volz,
 509 M Weber, and Harald Weinfurter. Towards long-distance
 510 atom-photon entanglement. *Physical Review Letters*,
 511 101(26):260403, 2008.
- 512 [30] John F. Clauser, Michael A. Horne, Abner Shimony,
 513 and Richard A. Holt. Proposed experiment to test lo-
 514 cal hidden-variable theories. *Physical Review Letters*,
 515 23:880–884, Oct 1969.
- 516 [31] Marek Zukowski, Anton Zeilinger, and Harald Wein-
 517 furter. Entangling photons radiated by independent
 518 pulsed sources. *Annals of the New York academy of Sci-*
 519 *ences*, 755(1):91–102, 1995.
- 520 [32] Matthias Körber, Olivier Morin, Stefan Langenfeld, An-
 521 dreas Neuzner, Stephan Ritter, and Gerhard Rempe.
 522 Decoherence-protected memory for a single-photon
 523 qubit. *Nature Photonics*, 12(1):18, 2018.

METHODS

Atom-photon entanglement distribution at telecom wavelength

The polarization-preserving quantum frequency conversion (QFC) devices used in this work are described in detail in references²¹ and³³. In contrast to previous work, here a more favourable pump–signal frequency combination is selected with respect to the Raman background: 1607 nm–1517 nm instead of 1600 nm–1522 nm. This increases the signal-to-background ratio (SBR) by a factor of 4 and allows to install a QFC device in Node 2—effectively doubling the background—while not being limited by the SBR.

Since the quality of the entanglement shared between the two nodes directly depends on the fidelity of the two entangled atom-photon pairs, we individually characterize the atom-photon entanglement generated in both nodes. The generated states are analysed using the same fibre configurations and atomic readout times as during the atom-atom entanglement measurements presented in the main text. For an overview see Table I. Note that an high fidelity atomic state readout can only be made after a full oscillation period of the atom in the dipole trap, which equals 14.3 μs and 17.8 μs for Node 1 and 2, respectively.

TABLE I. Long fibre configurations and corresponding atomic readout times. The fibre link lengths and corresponding atomic readout times for the experiments presented in the main text and the atom-photon characterization measurements. L_1 (L_2) equals the fibre length between Node 1 (Node 2) and the middle station. A_1 (A_2) gives the attenuation in the fibre network between the node and the middle station, this includes inefficiencies of fibre-to-fibre connectors.

L (km)	L_1 (km)	L_2 (km)	A_1 (dB)	A_2 (dB)	t_1 (μs)	t_2 (μs)
6	2.6	3.3	-0.7	-0.8	28.5	35.5
11	5.4	5.5	-1.5	-1.3	57.1	71.0
23	11.3	11.4	-3.3	-2.8	114.2	124.3
33	16.5	16.6	-4.5	-4.1	171.2	177.5

The atom-photon entanglement fidelity is analysed following the methods in Ref.²¹, whereby the atomic readout time is now delayed to allow for two-way communication to the middle station for each node over the respective fibre length. The polarization of the photons are measured in two bases, H/V (horizontal/vertical) and D/A (diagonal/anti-diagonal), i.e., X and Y, while the atomic analysis angle was rotated over angles including these bases. The atom-photon state correlations are shown for Node 1 in Fig. 5 and for Node 2 in Fig. 6.

For the fibre configuration $L = 6$ km, i.e., $L_1 = 2.6$ km and $L_2 = 3.3$ km, we find atom-photon state fidelities of 0.941(5) for Node 1 and 0.911(6) for Node 2, relative to a maximally entangled state, which are mainly limited by the atomic state readout and entanglement generation fidelity. For longer fibre lengths the entangled state

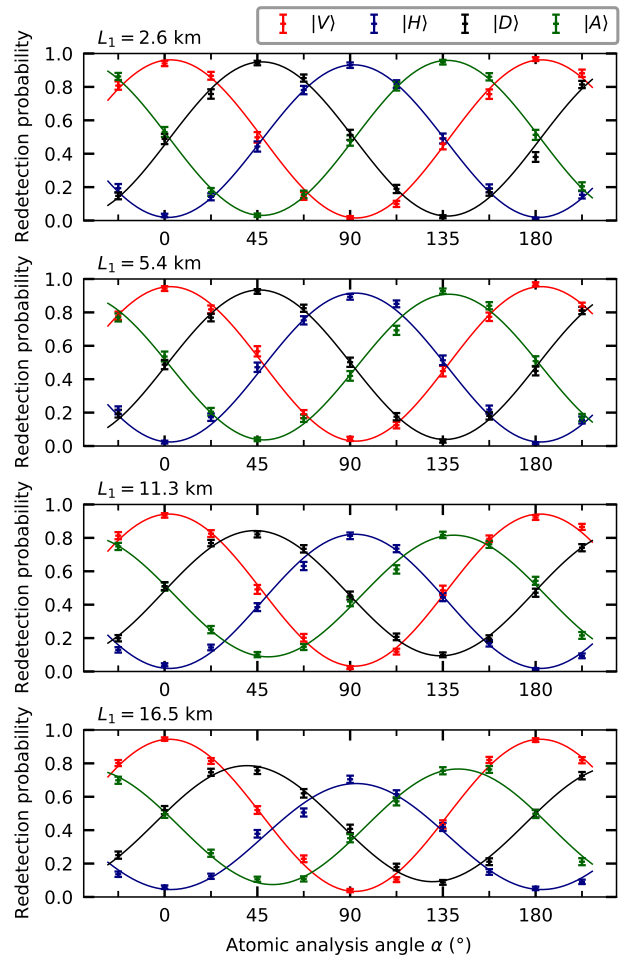


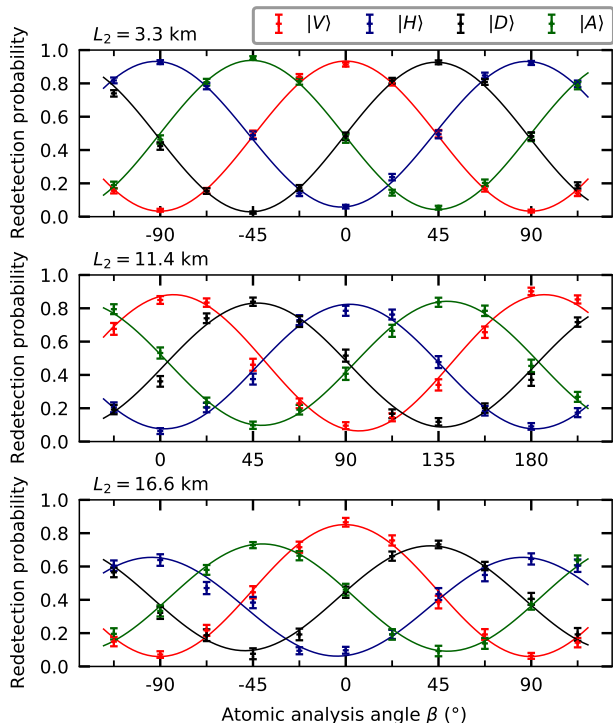
FIG. 5. Atom-photon entanglement distribution for Node 1. The measurements include an atomic readout delay to allow for two-way communication with the middle station. The error bars indicate statistical errors of one standard deviation.

decoherence due to magnetic field fluctuations along the guiding field and the position-dependent dephasing.

Modelling of the quantum memory decoherence

In both nodes, a single ^{87}Rb atom is stored in an optical dipole trap, where a qubit is encoded into the states $5^2S_{1/2} |F = 1, m_F = \pm 1\rangle$. The dipole trap is operated at $\lambda_{\text{ODT}} = 850$ nm with typical trap parameters of, e.g., for Node 1, a trap depth $U_0 = 2.32$ mK and beam waist $\omega_0 = 2.05 \mu\text{m}$. The qubit evolves effectively in a spin-1 system since the state $5^2S_{1/2} |F = 1, m_F = 0\rangle$ could also be populated. The state fidelity is influenced by two factors: the first one is the AC-stark shift originating from the dipole trap and, secondly, the Zeeman effect arising from magnetic fields.

To model the dephasing of the quantum memories, we simulate the evolution of this spin-1 system while the atom is oscillating in the dipole trap, affected by longi-



565

566 FIG. 6. **Atom-photon entanglement distribution for**
 567 **Node 2.** The measurements include an atomic readout delay
 568 to allow for two-way communication with the middle station.

603 tudinal polarization components and external magnetic
 604 fields³⁴. For this, first, we randomly draw a starting po-
 605 sition and velocity of an atom from a 3D harmonic os-
 606 cillator distribution in thermal equilibrium. Second, the
 607 motion of the atom is simulated in a realistic Gaussian
 608 potential resulting in an atomic trajectory for which the
 609 evolution of the atomic state is calculated based on the
 610 local optically induced and external magnetic fields. Fi-
 611 nally, this is repeated for a large number of trajectories,
 612 whereby the averaged projection for all trajectories yields
 613 the simulation result.

621 The model takes the following independently measured
 622 inputs: (1) the trap geometry specified by the beam
 623 waist ω_0 , which is obtained from knife-edge measure-
 624 ments of the dipole trap beam focus in two dimensions³⁵;
 625 (2) the trap depth U_0 , determined via measurements of
 626 the transverse trap frequency using parametric heating³⁶
 627 and the atomic state rephasing period³⁴; and (3) the
 628 atomic temperature T , modelled as a Boltzmann distri-
 629 bution which is measured via the release and recapture
 630 technique³⁷. Inputs 1 and 2 define the position, ampli-
 631 tude, and phase of the longitudinal polarization compo-
 632 nents, while inputs 1-3 characterize the atomic trajec-
 633 tories. Furthermore, we include a uniform magnetic field
 634 along three directions with additional shot-to-shot noise
 635 following Gaussian distributions.

636 Fig. 7 shows simulation results and measurement data

637 of the state evolution in Node 1 for varying state readout
 638 orientation and time. The model accurately predicts
 639 the evolution of the measured atomic states and shows
 640 that the memory storage time is limited by magnetic
 641 field fluctuations on the order of < 0.5 mG along the
 642 bias field direction in addition to the position-dependent
 643 dephasing due to the longitudinal field components of
 644 the strongly focussed dipole trap. The simulation results
 645 presented in the main text consider the envelope of the
 646 found oscillating state evolution in three bases.

647

648 Experimental sequence

649 The entanglement generation sequence is visualised in
 650 Fig.8. The sequence starts by trapping an atom in both
 651 nodes. For this, a single atom is loaded from a magneto-
 652 optical trap (MOT) into a tightly focussed dipole trap,
 653 which takes less than 1 second. Every entanglement gen-
 654 eration try consist of $3 \mu\text{s}$ optical pumping (80% effi-
 655 ciency) and an excitation pulse (Gaussian laser pulse
 656 with a FWHM of 21 ns) to generate atom-photon en-
 657 tanglement in the following decay. Subsequent to each
 658 try, a waiting time is implemented to cover the propa-
 659 gation time of the photons in the long fibres. After 40
 660 unsuccessful tries the atoms are cooled for $350 \mu\text{s}$ using
 661 polarization gradient cooling (PGC). The lifetime of the
 662 atoms in the trap during the entanglement generation
 663 process is approximately 5 seconds.

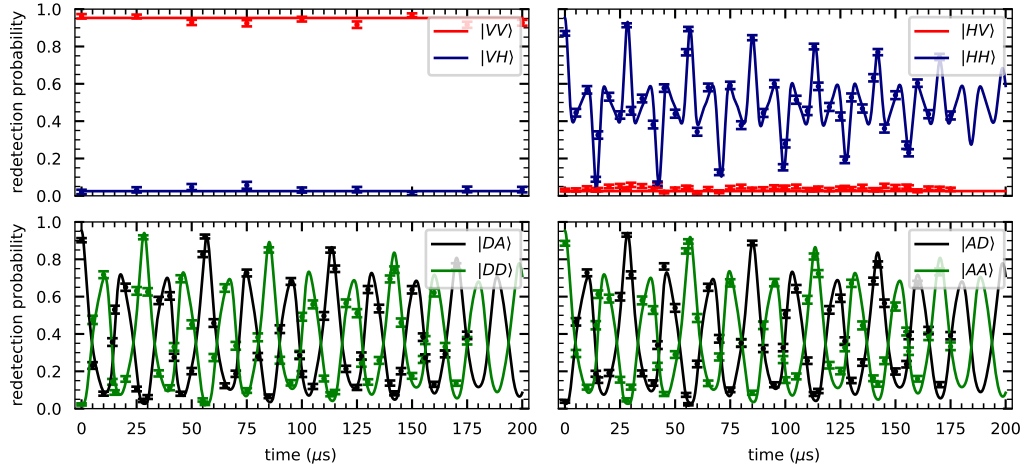
673 To verify if both traps still store a single atom, the
 674 entanglement generation process is interrupted after
 675 200 ms to check the presence of the atoms. For this,
 676 a microelectromechanical systems (MEMS) fibre-optic
 677 switch is implemented in each node at the SM-fibre
 678 originating from the atom trap. The switches guide the
 679 atomic fluorescence either to the QFC devices during
 680 the entanglement generation tries or to an avalanche
 681 photodiode (APD) located at each node during 40 ms
 682 of fluorescence collection. Note that the SNSPDs of the
 683 BSM cannot be used for this purpose since they are
 684 behind narrowband spectral filters.

685

686 Polarization control of long fibres

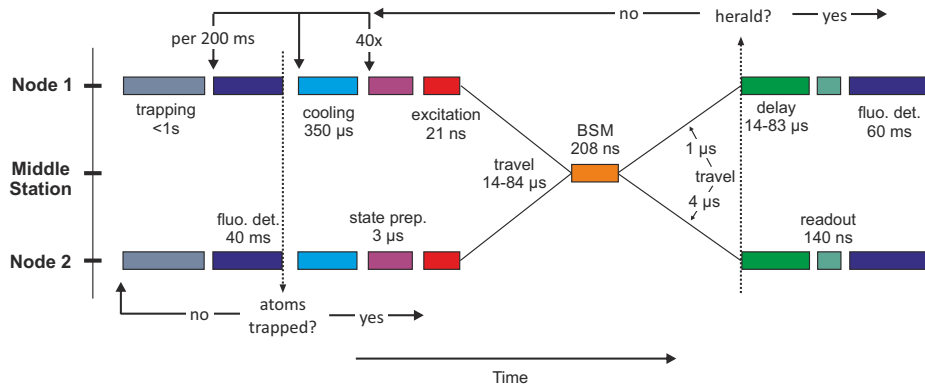
687 Polarization drifts in the long fibres are compensated for
 688 using an automated polarization control based on the
 689 method presented in Ref.²⁹. The polarization control is
 690 performed every 7 minutes, takes approximately 20 sec-
 691 onds, and is based on a gradient decent optimization al-
 692 gorithm. In this way, polarization errors are kept below
 693 1% during all measurements.

694 The fibre polarization is optimized using classical
 695 laser light at the single photon frequency whereby the
 696 polarization is alternated between vertical and diagonal
 697 linear polarizations at 10 Hz. The light is overlapped
 698 with the complete single photon path up to the detectors
 699 originating from Node 1 and Node 2. In both output
 700 arms of the BS a flip-mirror can reflect the classical light
 701 into a polarimeter during the optimization. Three fibre
 702 polarization controllers (PC) are connected to the fibre
 703 BS of the BSM: at both input ports and at one output



614

615 **FIG. 7. Atomic state evolution in two bases.** Atom-photon entanglement simulations (solid lines) and measurements
 616 (points) of Node 1 with photon detection at 780 nm using a 5 m long fibre. The atomic state readout orientation and time is
 617 varied to characterize the memory coherence. The labels in the legend indicate the $|atom\ photon\rangle$ state analysed. Simulation
 618 parameters: trap waist $2.05\mu\text{m}$, trap depth 2.32 mK, atom temperature $50\mu\text{K}$, bias field $B_y = 75.5\text{ mG}$, and field fluctuations
 619 $\Delta B_y = 0.5\text{ mG}$ Gaussian distributed. With these parameters, we observe de- and rephasing of the atomic state due to the
 620 longitudinal polarization components at the trap frequency of 70 kHz and a larmor precession at a frequency of 105 kHz.



664

665 **FIG. 8. Experimental sequence of the atom-atom entanglement generation.** In both nodes a single atom is trapped
 666 and cooled using polarization gradient cooling. Next, the entanglement generation tries start containing state preparation and
 667 synchronous excitation of the atoms. The atoms are re-cooled after 40 unsuccessful entanglement generation tries. The travel
 668 time of the photons to the middle station equals 14 to $84\ \mu\text{s}$, depending on the fibre length. With regard to the assumption
 669 that the heralding signal is communicated back to the nodes along fibres of respective lengths, an additional delay is included
 670 to account for the communication time from the middle station back to the nodes. After a $200\ \text{ms}$ interval of entanglement
 671 generation tries the presence of the atoms in the traps is checked using fluorescence collection with an APD (see text). The
 672 QFC takes place subsequent to the atomic excitation.

704 port.

705

706 Entanglement swapping fidelity

707 The single photons are detected with a Bell-state measurement device consisting of a fibre beamsplitter (BS),
 708 two polarizing beamsplitters (PBS) (Wollaston Prisms),
 709 two superconducting nanowire single photon detectors (SNSPD), as illustrated in Fig. 1 of the main text. In
 710 this setup, the fibre BS guarantees a unitary spatial overlap
 711 of the photons originating from the nodes, while the
 712
 713

714 PBSs and single photon detectors allow for polarization
 715 analysis in both output ports. The detectors, labelled
 716 $H_1, V_1, H_2,$ and V_2 , are not photon number resolving,
 717 and hence coincidences events in six detector pairs can
 718 be registered, see Tab. II. For the purpose of a Bell-state
 719 measurement, we can categorize these combinations into
 720 three groups: D_+, D_- , and D_\emptyset . Here, detector combinations in group D_+ and D_- herald the Bell states $|\Psi^+\rangle$
 721 and $|\Psi^-\rangle$, respectively, while combinations in group D_\emptyset
 722 should not occur for perfectly interfering photons and are
 723

discarded in the analysis. However, the relative occurrence of these events is used in the following to quantify the two-photon interference contrast.

For not interfering photons, two-photon events are evenly distributed between the 16 possible detector combinations (not considering experimental imperfections). Since the order of the detector combination is not of interest, e.g., (V_1, H_1) is similar to (H_1, V_1) , we end up with 10 distinct coincidences and their probabilities, as listed in Tab. II. For perfectly interfering photons the probabilities differ: the probability to detect the D_\emptyset group vanishes and all four Bell states are detected with a probability of $1/4$, whereby the $|\Phi^\pm\rangle$ Bell states fall into the group 'not detected' for the employed setup.

The two-photon interference contrast is defined as⁶

$$C = 1 - \frac{2N_{D_\emptyset}}{N_{D_+} + N_{D_-}}, \quad (2)$$

where N_k is the number of events in detection group k . With this definition and the probabilities of the different coincidences, the contrast equals zero for not interfering photons and one for perfectly interfering photons. See Ref.³⁸ for a thorough analysis of the two-photon interference contrast and entanglement swapping fidelity, including experimental imperfections.

The interference contrast is measured as follows. During measurement runs all single-photon detection events are recorded, which allows to count the number of occurrences of the coincidence events for all three detection groups. Next, the the interference contrast is evaluated using equation (2). To verify this method, we additionally evaluate the contrast of not interfering photons. This is done by analysing coincidence detections of two photons originating from distinct entanglement generation tries. In this way, the photons did not interfere since the photon wave-packages are completely separated in time. Fig. 2b of the main text shows exactly this for the $L = 6$ km measurement. Shown are the normalized wrong coincidences, defined as $1 - C$, for varying

time differences between the photons ($\Delta\tau$). Note that the horizontal spacing of the measurement times equals the repetition rate of the entanglement generation tries.

The entanglement swapping fidelity is mainly limited by two effects. First, by experimental imperfections that reduce the indistinguishability of the two photons, e.g., as discussed in the main text, by a not perfect time overlap of the two photon wave-packets. Second, by double excitations due to the finite duration of the excitation pulse. For a detailed description see Ref.³⁹.

DATA AVAILABILITY

The datasets generated during and/or analysed during the current study are available from the corresponding author on reasonable request.

CODE AVAILABILITY

The code supporting the plots within this paper is available from the corresponding authors upon reasonable request.

COMPETING INTERESTS

The authors declare no competing interests.

ACKNOWLEDGEMENTS

M.B. acknowledges the hospitality of the LMU group during multiple stays. We acknowledge helpful discussions with Stephan Kucera. We acknowledge funding by the German Federal Ministry of Education and Research (Bundesministerium für Bildung und Forschung (BMBF)) within the projects Q.com.Q and Q.Link.X (Contracts No. 16KIS0127, 16KIS0123, 16KIS0864, and 16KIS0880), the Deutsche Forschungsgemeinschaft (DFG, German Research Foundation) under Germany's Excellence Strategy – EXC-2111 – 390814868, and the Alexander von Humboldt foundation.

[33] Matthias Bock. Polarization-preserving quantum frequency conversion for trapped-atom based quantum networks. PhD thesis, Universität des Saarlandes, 2021.

[34] D. Burchardt. A rigorous test of bell's inequality and quantum teleportation employing single atoms. PhD thesis, Ludwig-Maximilians-Universität München, 2017.

[35] R. Garthoff. Efficient single photon collection for single atom quantum nodes. PhD thesis, Ludwig-Maximilians-Universität München, 2021.

[36] Wolfgang Alt, Dominik Schrader, Stefan Kuhr, Martin Müller, Victor Gomer, and Dieter Meschede. Single atoms in a standing-wave dipole trap. *Physical Review A*, 67(3):033403, 2003.

[37] Charles Tuchendler, Andrew Matheson Lance, Antoine Browaeys, Yvan RP Sortais, and Philippe Grangier. Energy distribution and cooling of a single atom in an optical tweezer. *Physical Review A*, 78(3):033425, 2008.

[38] Julian Hofmann. Heralded Atom-Atom Entanglement. PhD Thesis, Ludwig-Maximilians-Universität München, 2014.

[39] Wei Zhang, Tim van Leent, Kai Redeker, Robert Garthoff, Rene Schwonnek, Florian Fertig, Sebastian Eppelt, Wenjamin Rosenfeld, Valerio Scarani, Charles C-W Lim, and Harald Weinfurter. Experimental device-independent quantum key distribution between distant users. *arXiv preprint arXiv:2110.00575*, 2021.

770 TABLE II. **Possible two-photon coincidences.** The probabilities of the events are given for not interfering photons and for
 771 perfectly interfering photons.

	detection	coincidence	no interference	perfect interference
772	not detected	H ₁ ,H ₁	1/16	1/8
		H ₂ ,H ₂	1/16	1/8
		V ₁ ,V ₁	1/16	1/8
		V ₂ ,V ₂	1/16	1/8
773	D _∅ → discarded	H ₁ ,H ₂	1/8	0
		V ₁ ,V ₂	1/8	0
774	D ₊ → Ψ ⁺ ⟩	H ₁ ,V ₁	1/8	1/8
		H ₂ ,V ₂	1/8	1/8
775	D ₋ → Ψ ⁻ ⟩	H ₁ ,V ₂	1/8	1/8
		V ₁ ,H ₂	1/8	1/8

776